Geochemistry Geophysics Geosystems G3
AN ELECTRONIC JOURNAL OF THE EARTH SCIENCES
Published by AGU and the Geochemical Society

Article
Volume 6, Number 3
18 March 2005
Q03008, doi:10.1029/2004GC000828
ISSN: 1525-2027

Quantifying magmatic, crustal, and atmospheric helium contributions to volcanic aquifers using all stable noble gases: Implications for magmatism and groundwater flow

M. O. Saar
Geological Sciences, University of Michigan, 2534 C. C. Little Building, 425 E. University, Ann Arbor, Michigan 48109-1063, USA (msaar@umich.edu)

Now at Department of Geology and Geophysics, University of Minnesota, 310 Pillsbury Drive, S. E., Minneapolis, Minnesota 55455, USA (saar@umn.edu)

M. C. Castro and C. M. Hall
Geological Sciences, University of Michigan, 2534 C. C. Little Building, 425 E. University, Ann Arbor, Michigan 48109-1063, USA

M. Manga
University of California, Berkeley, California, USA

T. P. Rose
Lawrence Livermore National Laboratory, Livermore, California, USA

[1] We measure all stable noble gases (He, Ne, Ar, Kr, Xe) in spring waters in the Oregon Cascades volcanic arc and in eastern Oregon, USA. We show that in order to estimate magmatic helium (He) contributions it is critical to simultaneously consider He isotopic ratios, He concentrations, and mixing of He components. Our component mixing analysis requires consideration of all measured noble gases but no other elements and is particularly insightful when strong dilution by air-saturated water has occurred. In addition, this approach can allow distinction between crustal and magmatic He components and facilitates their identification in deep groundwaters that have been diluted by near-surface water. Using this approach, we show that some cold springs on the eastern flanks of the Oregon Cascades exhibit He isotopic ratios that indicate significant magmatic He contributions comparable to those observed in thermal springs on the western flanks. Furthermore, while these magmatic He contributions are largest in deep groundwaters near the Cascades crest, greater magmatic excess He fractions than may be inferred from He isotopic ratios alone are present in all (deep) groundwaters including those at larger distances (>70 km) from the volcanic arc. We also suggest that excess He and heat discharge without dilution by air-saturated water may be restricted to spring discharge along faults.

Components: 9865 words, 7 figures, 3 tables.

Keywords: magmatic helium; component mixing; hot springs; Cascades; atmospheric helium; Basin and Range.

Index Terms: 1034 Geochemistry: Hydrothermal systems (0450, 3017, 3616, 4832, 8135, 8424); 1041 Geochemistry: Stable isotope geochemistry (0454, 4870); 1829 Hydrology: Groundwater hydrology; 1832 Hydrology: Groundwater transport; 8424 Volcanology: Hydrothermal systems (0450, 1034, 3017, 3616, 4832, 8135).

Received 27 August 2004; **Revised** 5 November 2004; **Accepted** 17 December 2004; **Published** 18 March 2005.

Saar, M. O., M. C. Castro, C. M. Hall, M. Manga, and T. P. Rose (2005), Quantifying magmatic, crustal, and atmospheric helium contributions to volcanic aquifers using all stable noble gases: Implications for magmatism and groundwater flow, *Geochem. Geophys. Geosyst.*, *6*, Q03008, doi:10.1029/2004GC000828.

1. Introduction

[2] Heat flow and magmatic volatile fluxes such as helium (He) are often used to infer the extent of magma intrusions, groundwater flow patterns, and advective heat transfer in magmatically active regions [e.g., *Ingebritsen et al.*, 1994; *Rose and Davisson*, 1996; *James et al.*, 2000; *Evans et al.*, 2004; *Saar and Manga*, 2004; S. Hurwitz et al., Systematics of halogen elements and their isotopes in thermal springs of the Cascade Range, Central Oregon, Western USA, submitted to *Earth and Planetary Science Letters*, 2005].

[3] He isotope concentrations in groundwaters often exceed those expected for water in solubility equilibrium with the atmosphere, hereafter referred to as He_{eq} from air-saturated water (ASW). These excesses can result from different sources: (1) an excess air (A_{ea}) He component (He_{ea}) from dissolution of small air bubbles caused by fluctuations of the groundwater table; (2) β-decay of natural and bomb tritium (tritiogenic ^3He_t); (3) the $^6Li(n, \alpha)^3H(^3He)$ reaction (nucleogenic ^3He); (4) α-decay of the natural U and Th decay series elements in crustal rocks (radiogenic ^4He); and (5) mantle and magmatic contributions to both ^3He and ^4He. Helium isotopes dissolved in groundwater are useful indicators of geologic processes and groundwater dynamics because atmospheric, crustal, and mantle He components display distinct $^3He/^4He$ ratios (R). Typically, He produced in the crust results in $0.02 \leq R_c/R_a \leq 0.05$ [e.g., *Castro*, 2004] while mantle-derived He is characterized by $8 \leq R_m/R_a \leq 30$ [e.g., *Graham*, 2002], where $R_a = 1.384 \times 10^{-6}$ [*Clarke et al.*, 1976] is the atmospheric ratio.

[4] Significant crustal and mantle-derived magmatic helium components in groundwater can be masked however by mixing with shallow waters that contain atmospheric He. This dilution of crustal and magmatic He signals can be accounted for by quantifying and removing total dissolved atmospheric helium components,

$$He_{da} = He_{eq} + He_{ea}, \quad (1)$$

from total measured He concentrations (He_{meas}). The following two paragraphs briefly introduce two methods for estimating He_{da}. Both approaches are discussed in more detail in sections 6.1 and 6.2.

[5] He_{da} is commonly estimated based on the helium to neon ratio, assuming that all neon (Ne) is of atmospheric origin and that He_{da} results either entirely from He_{eq} or entirely from He_{ea} [e.g., *Hilton*, 1996]. In addition, if total He/Ne ratios are less than about four times those of the atmosphere, measurements of the total nitrogen to argon ratios (N_2/Ar) are required to infer He_{eq} versus He_{ea} [e.g., *Hilton*, 1996].

[6] Here, we constrain He_{eq} and He_{ea} by analyzing the noble gases neon (Ne), argon (Ar), krypton (Kr), and xenon (Xe), as described in detail by *Ballentine and Hall* [1999]. This method provides a means to detect diluted excess He components in groundwater and eliminates the need to measure nitrogen in addition to He, Ne, and Ar when estimating the components of He_{da} (equation (1)). Instead, measurements can be restricted to noble gases by including Kr and Xe. In addition, combining results from the Ne, Ar, Kr, and Xe analysis with so-called He component mixing analyses (described in section 6.1) allows estimation of magmatic versus crustal excess He fractions. A similar combined approach has been applied to sedimentary systems [e.g., *Castro et al.*, 2000] but appears to be absent from volcanologically oriented helium studies.

[7] Through an example in the Oregon Cascades and the Basin and Range in the northwestern USA, we illustrate the practical gains achieved by applying this combined approach to a volcanic setting. Specifically, by revealing significant magmatic He contributions in some colder springs, this method provides additional insights regarding groundwater flow patterns as well as magmatic versus crustal excess helium signals.

2. Geologic and Hydrologic Background

[8] The High Cascades (Figures 1 and 2) in the Pacific Northwest (USA) consist primarily of active Quaternary stratovolcanoes of mostly basaltic to andesitic composition. Here, large groundwater recharge rates cause advective transfer of heat and

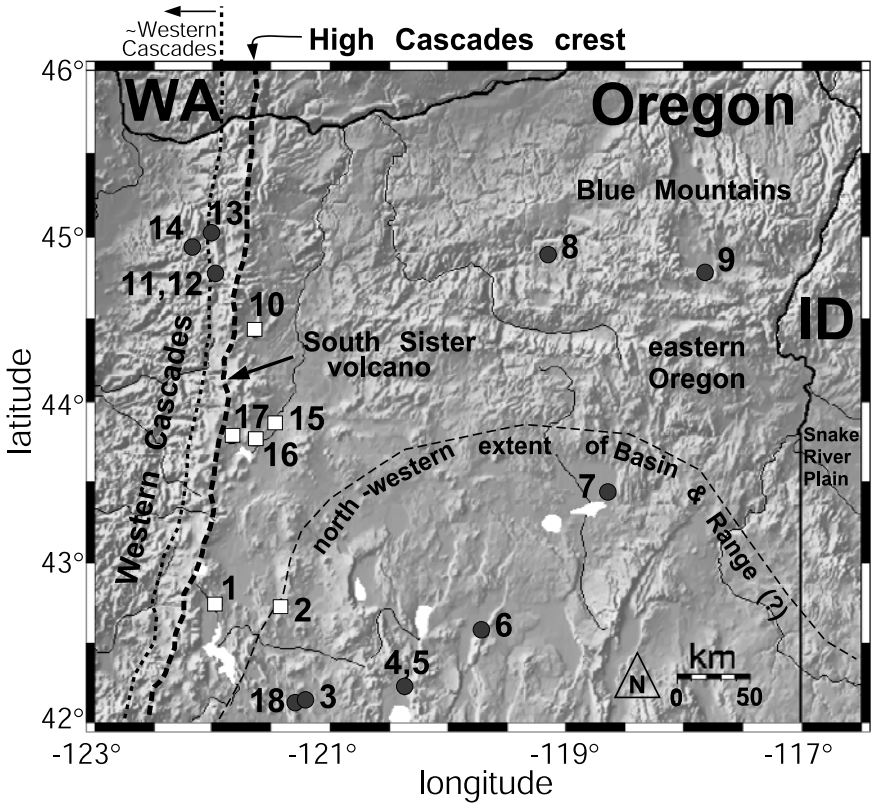

Figure 1. Shaded relief map of the study region and major tectonic provinces in Oregon, USA. Hot (>10°C) and cold (≤10°C) springs are indicated by gray circles and white squares, respectively. Spring numbers are keyed to Tables 2 and 3.

magmatic volatiles toward springs on the volcanoes' lower flanks [e.g., *Ingebritsen et al.*, 1994; *Manga*, 1998; *James et al.*, 2000; *Saar and Manga*, 2004]. In Oregon, the older Oligocene to lower Pliocene Western Cascades are underlain by less permeable rocks and are frequently separated from the High Cascades by normal faults [*Ingebritsen et al.*, 1994] (Figures 1 and 2). Faults east and west of the High Cascades form a graben in which springs typically discharge large volumes of cold water at the contact between permeable volcanic and less permeable sedimentary rocks [*James et al.*, 2000] (Figure 2). Discharge along faults near the Western Cascades typically produces hot springs. Crustal uplift of the western flanks of South Sister volcano (Figure 1) and high He isotopic ratios of up to 6.8 R_a [*Evans et al.*, 2004] have been attributed to recent magmatic activity. Figure 1 shows the northwestern extent of the Basin and Range tectonic province adjacent to

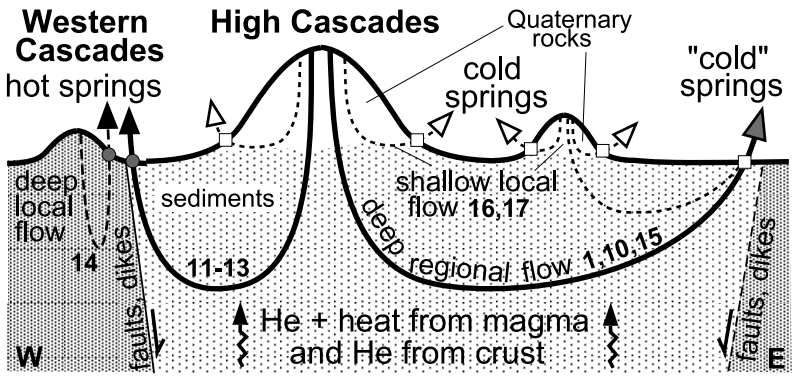

Figure 2. Conceptual model of the hydrothermal system beneath the Cascades (Figure 1). Numbers denote hot (gray circles) and cold (white squares) springs, as discussed in the main text and Table 3. "Cold" springs yield temperatures ≤10°C but show diluted magmatic heat and/or He discharge.

the Cascades. The Basin and Range results from extensional tectonics causing thinning and normal faulting of the crust leading to magmatism and high heat flow. Spring discharge in eastern Oregon is lower than in the Cascades.

3. Sampling Techniques and Experimental Methods

[9] Water samples were collected in copper tubes (i.e., standard refrigeration grade 3/8″ Cu tubing) from springs in the study area (Figure 1) after temperature, pH, and electrical conductivity reached equilibrium. While the water flushed through the system for approximately 10 min, the absence of gas bubbles that could potentially indicate gas fractionation in the samples was checked through a transparent plastic tube mounted at the end of the Cu tube. The Cu tubes were then sealed by stainless steel pinch-off clamps [*Weiss*, 1968]. We measured concentrations and isotopic ratios for all stable noble gases (He, Ne, Ar, Kr, and Xe) at the University of Michigan, as described briefly below and in detail in the appendices.

[10] Water samples in Cu tubes for analysis of He, Ne, Ar, Kr, and Xe were attached to an automated noble gas extraction and purification system built at the University of Michigan. The Cu tube is connected to a vacuum system and evacuated to below 2×10^{-3} Torr. The bottom clamp is then opened, releasing the water into a low He diffusion glass flask. Extraction of the dissolved gases occurs in two stages: the first uses water vapor as a carrier gas to transport all dissolved gases through a tubing constriction into a liquid N_2 cold trap; the second stage uses water vapor from warming the small quantity of water in the cold trap to transport the dissolved gases into a section of the system with a 3 Å molecular sieve. This part of the system is dried by the water adsorption properties of the molecular sieve, and the gases from the water sample can then be admitted into a clean-up section equipped with getter pumps to remove all active gases. Separation of noble gases are performed in this section using a computer-controlled cryo-separator.

[11] The complete measurement procedure involves estimating the concentration of each noble gas component, measuring the isotopic ratios for Ne, Ar, Kr, and Xe, then the measurement of the $^3He/^4He$ ratio. First, a portion of a known volume of air is introduced to the molecular sieve section of the extraction system, and all noble gases are measured in turn with a MAP 215 mass spectrometer. This calibrates the mass spectrometer signal size for each noble gas. Subsequent to the air calibration run, the exact same measurement procedure is performed on a portion of the unknown sample. The remainder of the unknown is then analyzed for He isotope ratios. Finally, He from another air reservoir sample is inlet into the mass spectrometer and that is used to calibrate R_a. ^4He and all Ne and Ar isotopes are measured using a Faraday detector. ^3He and all Kr and Xe isotopes are measured using an electron multiplier in ion counting mode. Further details regarding the noble gas extraction and purification lines as well as measurement techniques are provided in the appendices.

4. Helium Systematics

[12] Excess helium (He_{exc}) is estimated by removing the He_{eq} and He_{ea} components from total measured helium (He_{meas}). He_{exc} comprises both magmatic (He_m) and crustal ($He_c = He_{cin} + He_{cext}$) components, where He_{cin} and He_{cext} are produced in situ within the aquifer and externally at greater depths, respectively, so that

$$\begin{aligned} {}^3He_{exc} &= {}^3He_{meas} - {}^3He_{eq} - {}^3He_{ea} \\ &= {}^3He_{cin} + {}^3He_{cext} + {}^3He_m + {}^3He_t \end{aligned} \quad (2)$$

and

$$\begin{aligned} {}^4He_{exc} &= {}^4He_{meas} - {}^4He_{eq} - {}^4He_{ea} \\ &= {}^4He_{cin} + {}^4He_{cext} + {}^4He_m. \end{aligned} \quad (3)$$

We also specify

$$He_{noea} = He_{meas} - He_{ea}. \quad (4)$$

Concentrations of helium-3 isotopes in equation (2) are given by $^3He_{eq} = {}^4He_{eq} \times R_{eq}$, $^3He_{ea} = {}^4He_{ea} \times R_a$, and $^3He_{meas} = {}^4He_{meas} \times R_{meas}$, where $R_{eq} = (1.360 \pm 0.006) \times 10^{-6}$ [*Benson and Krause*, 1980] and R_{meas} are the $^3He/^4He$ ratios for ASW and total measured He, respectively (Table 1). Furthermore, we define

$$R_{noea} = \frac{{}^3He_{noea}}{{}^4He_{noea}} \quad (5)$$

and

$$R_{exc} = \frac{{}^3He_{exc}}{{}^4He_{exc}}. \quad (6)$$

5. Results

[13] Noble gas concentrations and He isotope ratios, as well as spring names, locations, elevations,

Table 1. Definition of Symbols in Equations

Symbol[a]	Definition	Units	Description
A_{ea}[b]		cm^3 STP/g	excess air (bubbles) introduced by fluctuations of the water table
β	$= \beta_{Ne}/\beta_{He}$		ratio of Ne to He Bunsen coefficients
β_{He}		cm^3 STP/g	Bunsen coefficient for solubility of He in water
β_{Ne}		cm^3 STP/g	Bunsen coefficient for solubility of Ne in water
f_m[c]			magmatic excess He fraction
$1 - f_m$[c]			crustal excess He fraction
F_{He}[d]	$= (5.24 \pm 0.05) \times 10^{-6}$		volume fraction of He in dry air
F_{4He}	$\approx F_{He}$		volume fraction of ^4He in dry air
He_a		cm^3 STP/g	helium concentration in the atmosphere
He_{da}[b]	$= He_{eq} + He_{ea}$	cm^3 STP/g	dissolved atmospheric He from both He_{eq} and He_{ea}
He_{ea}	$= A_{ea}\, F_{He}$	cm^3 STP/g	dissolved atmospheric He from excess air (A_{ea})
He_{eq}	$= He_{da} - He_{ea}$	cm^3 STP/g	dissolved atmospheric He from air-saturated water (ASW)
He_{exc}	$= He_{meas} - He_{eq} - He_{ea}$	cm^3 STP/g	excess He, i.e., without any dissolved atmospheric He
	$= He_{cin} + He_{cext} + He_m + {}^3He_t$	cm^3 STP/g	excess He, i.e., from crustal, magmatic, and tritiogenic ^3He
He_c	$= He_{cin} + He_{cext}$	cm^3 STP/g	crustal He from both He_{cin} and He_{cext}
He_{cin}		cm^3 STP/g	crustal He from production within aquifer
He_{cext}		cm^3 STP/g	crustal He from production external to aquifer at greater depth
He_m		cm^3 STP/g	magmatic He (derived from the mantle and possibly some crustal He)
He_{meas}	$\approx {}^4He_{meas}$	cm^3 STP/g	measured total He (without any corrections)
He_{noea}	$= He_{meas} - He_{ea}$	cm^3 STP/g	measured He without excess air He component
^3He_t		cm^3 STP/g	tritiogenic helium-3 from the decay of natural bomb tritium
$^3He_{ea}$	$= {}^4He_{ea}\, R_a$	cm^3 STP/g	dissolved atmospheric helium-3 from excess air (A_{ea})
$^3He_{eq}$	$= {}^4He_{eq}\, R_{eq}$	cm^3 STP/g	dissolved atmospheric helium-3 from air-saturated water (ASW)
$^3He_{meas}$	$= {}^4He_{meas}\, R_{meas}$	cm^3 STP/g	measured total helium-3 (without any corrections)
$^4He_{da}$	$\approx He_{da}$	cm^3 STP/g	dissolved atmospheric helium-4 from both $^4He_{eq}$ and $^4He_{ea}$
$^4He_{ea}$	$= A_{ea}\, F_{4He}$	cm^3 STP/g	dissolved atmospheric helium-4 from excess air (A_{ea})
$^4He_{eq}$	$= {}^4He_{da} - {}^4He_{ea}$	cm^3 STP/g	dissolved atmospheric helium-4 from air-saturated water (ASW)
$^4He_{meas}$	$\approx He_{meas}$	cm^3 STP/g	measured total helium-4 (without any corrections)
Λ	$= (He_{meas}/Ne_{meas})/(He_a/Ne_a)$		measured total He/Ne ratio normalized by the one for the atmosphere
Ne_a		cm^3 STP/g	neon concentration in the atmosphere
Ne_{meas}	$\approx {}^4He_{meas}$	cm^3 STP/g	measured total neon (without any corrections)
R	$= {}^3He/{}^4He$		ratio of helium-3 to helium-4
R_a[e]	$= {}^3He_a/{}^4He_a$		ratio of helium-3 to helium-4 in the atmosphere
	$= (1.384 \pm 0.006) \times 10^{-6}$		
R_c	$= {}^3He_c/{}^4He_c$		ratio of helium-3 to helium-4 in the crust
R_{eq}[f]	$= {}^3He_{eq}/{}^4He_{eq} = 0.983\ R_a$		ratio of helium-3 to helium-4 in air-saturated water at 18°C
R_{exc}	$= {}^3He_{exc}/{}^4He_{exc}$		ratio of excess helium-3 to excess helium-4
R_m	$= {}^3He_m/{}^4He_m$		ratio of helium-3 to helium-4 in magma or mantle
R_{meas}	$= {}^3He_{meas}/{}^4He_{meas}$		measured ratio of helium-3 to helium-4
R_{noea}	$= {}^3He_{noea}/{}^4He_{noea}$		measured ratio of helium-3 to helium-4 without excess air component
R_{cea}/R_a	$= ([\Lambda\ R_{meas}/R_a] - 1)/(\Lambda - 1)$		He/Ne-corrected R_{cea}/R_a ratios assuming contamination by He_{ea} only
R_{ceq}/R_a	$= ([\beta\Lambda\ R_{meas}/R_a] - 1)/(\beta\Lambda - 1)$		He/Ne-corrected R_{ceq}/R_a ratios assuming contamination by He_{eq} only

[a] When no superscripts are given for He concentrations, then the sum $He = {}^3He + {}^4He \approx {}^4He$ is implied.
[b] Determined using Ne, Ar, Kr, and Xe as discussed by *Ballentine and Hall* [1999].
[c] Determined by the combined approach that uses Ne, Ar, Kr, and Xe together with a He component mixing analysis.
[d] Value from *Ozima and Podosek* [2002].
[e] Value from *Clarke et al.* [1976].
[f] Value from *Benson and Krause* [1980].

and temperatures are given in Tables 2 and 3. In the following paragraphs we discuss briefly some specific results with respect to large atmospheric helium components.

[14] Samples 2 and 16 contain large excess air (A_{ea}) components. While sample 16 still yields typical ASW values because it contains little to no excess helium, its R_{noea}/R_a error bars are strongly amplified to meaningless values when calculating R_{exc}/R_a, as discussed in section 6.1. In contrast, sample 2 is ill-defined, resulting in a negative R_{noea}/R_a ratio after removing A_{ea}, a trend further amplified in the R_{exc}/R_a ratio. Consequently, sample 2 is excluded from our discussion.

[15] Table 3 also presents the ratio of dissolved atmospheric helium to total measured helium (He_{da}/He_{meas}), as well as

$$\Lambda = \frac{He_{meas}/Ne_{meas}}{He_a/Ne_a}, \quad (7)$$

where the subscript "a" denotes atmospheric values. Increasing amounts of atmospheric He contributions result in increasing He_{da}/He_{meas} ratios and decreasing Λ values. He_{da}/He_{meas} ratios show that all samples result in He_{da} values either below 10% or above 50% of He_{meas} with no intermediate atmospheric He contributions (Table 3). In addition, all samples with $He_{da}/He_{meas} > 0.5$ also show $\Lambda < 4$ and all samples with $He_{da}/He_{meas} < 0.1$ indicate $\Lambda \gg 4$ (Table 3). $\Lambda = 4$ was suggested by *Hilton* [1996] as an approximate cut-off value below which separation of ASW versus A_{ea} derived He components is critical to avoid overestimation or underestimation of He_{exc}.

6. Discussion

[16] We begin this discussion by presenting (1) our combined approach that uses Ne, Ar, Kr, and Xe together with a He component mixing analysis to constrain ASW versus A_{ea} derived atmospheric He (section 6.1); and (2) a comparison between the standard He/Ne correction and our combined approach (section 6.2). As shown later, our combined method is particularly important for some of the samples with $He_{da}/He_{meas} > 0.5$ and $\Lambda < 4$.

6.1. Combining Ne, Ar, Kr, and Xe Analyses With He Component Mixing

[17] To identify He contributions from the crust, magma, and the atmosphere and their potential mixing, we first use Ne, Ar, Kr, and Xe to determine He_{eq} and He_{ea} [*Ballentine and Hall*, 1999] and associated He_{noea}, He_{exc}, R_{noea}, and R_{exc} values, as defined in section 4. Second, we apply these He isotopic concentrations and ratios to a component mixing analysis by employing a slightly modified method from *Weise and Moser* [1987] where equations (2) through (6) are combined to

$$R_{noea}/R_a = \frac{{}^4He_{eq}R_{eq} + {}^4He_{exc}R_{exc} + {}^3He_t}{{}^4He_{noea}\ R_a} \quad (8)$$

and then rearranged to

$$R_{noea}/R_a = (BX + R_{exc})/R_a. \quad (9)$$

Here,

$$B = R_{eq} - R_{exc} + {}^3He_t/{}^4He_{eq}, \quad (10)$$

$$X = {}^4He_{eq}/{}^4He_{noea}, \quad (11)$$

and

$$R_{exc} = f_m R_m + (1 - f_m)R_c, \quad (12)$$

where f_m and $1 - f_m$ are the magmatic and crustal excess helium fractions of the magmatic ($R_m = {}^3He_m/{}^4He_m$) and crustal ($R_c = {}^3He_c/{}^4He_c$) end-member isotope ratios, respectively. Equation (9) is the equation for a line, normalized by R_a, with slope B/R_a, y-axis intercept R_{exc}/R_a, and x-axis values $0 \leq X \leq 1$. Binary mixing between ASW ($X = 1$) and water dominated by He_{exc} from the crust and/or the magma ($X \rightarrow 0$) plots on a line (Figure 3).

[18] In contrast to previous studies, our equation (9) is normalized by R_a. This approach better illustrates our combined method because mixing lines readily serve as projection lines (discussed next) indicating the change in effective He isotope ratios when removing the ASW helium component (He_{eq}) from He_{noea}. Removing He_{eq} is equivalent to projecting the mean R_{noea}/R_a values and their error bars along mixing lines (Figure 3) onto the left y-axis where $X = 0$ and thus here $R_{noea}/R_a = R_{exc}/R_a$ as given by equation (9). As mixing lines diverge for $X \rightarrow 0$, error bars increase (see also two last columns in Table 3). Furthermore, largest corrections are applied to samples with large absolute slopes (positive or negative due to crustal or magmatic excess He, respectively) that have been diluted by ASW (plot toward the right y-axis of Figure 3). As a consequence of the previous two arguments, only samples 1, 10, and 15 show R_{exc}/R_a values

Table 2. Noble Gas Concentrations and Their 1σ Errors

Site	Spring Name[a]	Lat., deg	Long., deg	Elev., m	He_{meas}, cm^3 STP/g ±1.5%	Ne_{meas}, cm^3 STP/g ±1.5%	Ar_{meas}, cm^3 STP/g ±1.3%	Kr_{meas}, cm^3 STP/g ±1.3%	Xe_{meas}, cm^3 STP/g ±2.2%
01	Wood River	42.7376	−121.9778	1281	6.60×10^{-8}	2.03×10^{-7}	3.51×10^{-4}	9.04×10^{-8}	1.14×10^{-8}
02	Williamson River	42.7319	−121.4188	1424	3.78×10^{-7}	1.29×10^{-6}	9.46×10^{-4}	1.68×10^{-7}	1.78×10^{-8}
03	Twin Springs[b]	42.1333	−121.2197	1302	5.94×10^{-8}	1.77×10^{-7}	2.93×10^{-4}	6.73×10^{-8}	9.66×10^{-9}
04	Hunters' HS (n)	42.2215	−120.3699	1460	6.62×10^{-7}	7.62×10^{-8}	7.48×10^{-5}	1.36×10^{-8}	1.86×10^{-9}
05	Hunters' HS (s)	42.2214	−120.3698	1458	5.95×10^{-8}	1.02×10^{-7}	1.08×10^{-4}	2.03×10^{-8}	2.53×10^{-9}
06	Antelope HS	42.5745	−119.7113	1825	4.36×10^{-6}	1.20×10^{-7}	2.66×10^{-4}	6.95×10^{-8}	1.07×10^{-8}
07	Crane HS	43.4410	−118.6393	1266	3.27×10^{-6}	1.31×10^{-7}	2.41×10^{-4}	6.03×10^{-8}	8.86×10^{-9}
08	Ritter HS	44.8928	−119.1428	788	1.30×10^{-5}	2.62×10^{-7}	3.34×10^{-4}	7.81×10^{-8}	1.16×10^{-8}
09	Sam-O HS	44.7794	−117.8119	1056	5.62×10^{-6}	2.82×10^{-7}	3.24×10^{-4}	8.06×10^{-8}	1.17×10^{-8}
10	Metolius River	44.4348	−121.6382	1017	5.80×10^{-8}	1.77×10^{-7}	3.24×10^{-4}	7.93×10^{-8}	1.11×10^{-8}
11	Breitenbush HS (l)	44.7817	−121.9763	678	7.87×10^{-7}	8.74×10^{-8}	9.22×10^{-5}	1.87×10^{-8}	2.83×10^{-9}
12	Breitenbush HS (u)	44.7815	−121.9761	686	8.47×10^{-7}	1.04×10^{-7}	1.12×10^{-4}	2.38×10^{-8}	3.41×10^{-9}
13	Austin HS	45.0186	−122.0032	522	3.56×10^{-6}	7.05×10^{-8}	1.40×10^{-4}	3.64×10^{-8}	6.06×10^{-9}
14	Bagby HS	44.9344	−122.1735	697	1.02×10^{-6}	1.76×10^{-7}	3.12×10^{-4}	7.77×10^{-8}	1.19×10^{-8}
15	Spring River	43.8701	−121.4699	1274	7.10×10^{-8}	1.70×10^{-7}	3.31×10^{-4}	8.23×10^{-8}	1.30×10^{-8}
16	Fall River	43.7680	−121.6334	1311	4.87×10^{-8}	2.05×10^{-7}	3.67×10^{-4}	9.86×10^{-8}	1.27×10^{-8}
17	Quinn River	43.7836	−121.8372	1374	5.77×10^{-8}	2.12×10^{-7}	3.71×10^{-4}	8.98×10^{-8}	1.43×10^{-8}
18	Oregon HS	42.1159	−121.2890	1265	1.73×10^{-6}	7.73×10^{-8}	9.19×10^{-5}	1.96×10^{-8}	2.99×10^{-9}
	ASW[c]			0	4.41×10^{-8}	1.78×10^{-7}	2.84×10^{-4}	6.22×10^{-8}	8.3×10^{-9}

[a] Letters indicate n = northern, s = southern, l = lower, and u = upper. HS = Hot Spring(s).
[b] Inofficial working title of these springs.
[c] For comparison: air-saturated water (ASW) at 1 atm pressure and a temperature of 25°C [*Ozima and Podosek*, 2002].

Table 3. Data for All Oregon Springs Sampled Between 5 August and 13 August 2003 for This Study[a]

Site	Elev., m	T,[c] °C	He_{da}/He_{meas}	Λ	$^4He_{meas}$,[d] cm^3 STP/g	$^3He = {}^4He_{meas}R_{meas}$,[e] cm^3 STP/g	R_{meas}/R_a[e]	From He/Ne Correction		From Using Ne, Ar, Kr, and Xe[b]	
								R_{cea}/R_a[e]	R_{ceq}/R_a[e]	R_{noea}/R_a[e]	R_{exc}/R_a[e]
01	1281	10	0.730 > 0.5	1.13 < 4	6.58×10^{-8}	$(1.25 \pm 0.11) \times 10^{-13}$	1.37 ± 0.12	4.24 ± 0.29	1.47 ± 0.12	1.44 ± 0.22	2.42 ± 0.63
02	1424	10	0.965 > 0.5	1.02 < 4	3.78×10^{-7}	$(2.97 \pm 0.23) \times 10^{-13}$	0.57 ± 0.04	−23.6 ± 1.45[f]	0.45 ± 0.03	−2.18 ± 1.00[f]	−11.2 ± 7.0[f]
03	1302	24.7	0.717 > 0.5	1.17 < 4	5.94×10^{-8}	$(8.93 \pm 0.56) \times 10^{-14}$	1.09 ± 0.07	1.60 ± 0.08	1.11 ± 0.07	1.09 ± 0.09	1.34 ± 0.28
04	1460	76	0.048 < 0.1	30.1 ≫ 4	6.62×10^{-7}	$(1.09 \pm 0.07) \times 10^{-12}$	1.19 ± 0.07	1.19 ± 0.06	1.19 ± 0.08	1.19 ± 0.08	1.20 ± 0.08
05	1458	70	0.568 > 0.5	2.03 < 4	5.95×10^{-8}	$(9.10 \pm 0.85) \times 10^{-14}$	1.11 ± 0.10	1.21 ± 0.09	1.12 ± 0.09	1.11 ± 0.12	1.27 ± 0.28
06	1825	38.4	0.006 < 0.1	126 ≫ 4	4.36×10^{-6}	$(4.11 \pm 0.37) \times 10^{-12}$	0.68 ± 0.06	0.68 ± 0.05	0.68 ± 0.06	0.68 ± 0.06	0.68 ± 0.06
07	1266	>70[g]	0.009 < 0.1	86.5 ≫ 4	3.27×10^{-6}	$(2.67 \pm 0.18) \times 10^{-12}$	0.59 ± 0.04	0.59 ± 0.03	0.59 ± 0.04	0.59 ± 0.04	0.59 ± 0.04
08	788	40.8	0.004 < 0.1	173 ≫ 4	1.30×10^{-5}	$(1.07 \pm 0.05) \times 10^{-11}$	0.60 ± 0.03	0.59 ± 0.02	0.59 ± 0.04	0.60 ± 0.03	0.60 ± 0.03
09	1056	26.2	0.013 < 0.1	69.2 ≫ 4	5.60×10^{-6}	$(1.32 \pm 0.09) \times 10^{-11}$	1.70 ± 0.12	1.71 ± 0.10	1.70 ± 0.12	1.70 ± 0.12	1.71 ± 0.12
10	1017	9.1	0.708 > 0.5	1.14 < 4	5.81×10^{-8}	$(1.30 \pm 0.11) \times 10^{-13}$	1.62 ± 0.13	6.05 ± 0.39	1.77 ± 0.14	1.64 ± 0.15	3.15 ± 0.52
11	678	76	0.039 < 0.1	31.2 ≫ 4	7.87×10^{-7}	$(3.08 \pm 0.22) \times 10^{-12}$	2.83 ± 0.20	2.89 ± 0.17	2.85 ± 0.20	2.82 ± 0.21	2.90 ± 0.22
12	686	64	0.038 < 0.1	28.3 ≫ 4	8.47×10^{-7}	$(2.30 \pm 0.15) \times 10^{-12}$	1.96 ± 0.12	2.00 ± 0.10	1.97 ± 0.13	1.96 ± 0.13	2.00 ± 0.13
13	522	85	0.005 < 0.1	175 ≫ 4	3.55×10^{-6}	$(2.59 \pm 0.12) \times 10^{-11}$	5.26 ± 0.22	5.29 ± 0.22	5.27 ± 0.31	5.23 ± 0.25	5.28 ± 0.25
14	697	55.8	0.039 < 0.1	20.2 ≫ 4	1.02×10^{-6}	$(1.64 \pm 0.12) \times 10^{-12}$	1.16 ± 0.08	1.16 ± 0.07	1.16 ± 0.08	1.16 ± 0.08	1.16 ± 0.09
15	1274	5.8	0.541 > 0.5	1.45 < 4	7.07×10^{-8}	$(2.85 \pm 0.14) \times 10^{-13}$	2.91 ± 0.13	7.20 ± 0.31	3.27 ± 0.20	2.91 ± 0.16	5.19 ± 0.37
16	1311	6.5	0.980 > 0.5	0.82 < 4	4.86×10^{-8}	$(7.63 \pm 0.94) \times 10^{-14}$	1.14 ± 0.14	0.37 ± 0.03	1.19 ± 0.12	1.16 ± 0.27	8.61 ± 14.2[h]
17	1374	3.8	0.860 > 0.5	0.94 < 4	5.74×10^{-8}	$(7.79 \pm 0.39) \times 10^{-14}$	0.98 ± 0.05	1.32 ± 0.06	0.98 ± 0.06	0.98 ± 0.08	0.95 ± 0.47
18	1265	60.5	0.015 < 0.1	77.8 ≫ 4	1.73×10^{-6}	$(2.90 \pm 0.28) \times 10^{-12}$	1.21 ± 0.11	1.21 ± 0.09	1.21 ± 0.10	1.21 ± 0.12	1.21 ± 0.12
ASW[i]	0	18			4.51×10^{-8}	$(6.13 \pm 0.03) \times 10^{-14}$	0.98 ± 0.01				

[a] Except when otherwise specified (see footnotes d and e below), 1σ errors are given implicitly by the number of significant digits. Helium isotope ratios, $R = {}^3He/{}^4He$, are normalized by the atmospheric value of $R_a = (1.384 \pm 0.006) \times 10^{-6}$ [*Clarke et al.*, 1976]. Parameters are further defined in the main text. Cold (≤10°C) springs (1, 2, 10, 15–17) and hot springs (3–9, 11–14, 18) are indicated by squares and circles, respectively, in Figures 1–6.

[b] Method described by *Ballentine and Hall* [1999].

[c] Spring discharge temperature.

[d] Standard error = 1.5% of value.

[e] Value is ±1σ standard error.

[f] This sample is ill-defined due to a large excess air component resulting in too large error bars and negative R_{cea}/R_a, R_{noea}/R_a, and R_{exc}/R_a, as further discussed in sections 5 and 6. The sample is thus omitted from the remainder of the discussion and from Figures 3–6.

[g] Maximum temperature reading of 70°C on temporary substitute thermometer.

[h] This sample contains significant excess air and little excess He so that error bars are large (Figure 3). It is essentially ASW and can thus only be shown in Figures 3 and 4a but not in Figures 4b, 5, and 6, as discussed in sections 5 and 6.1.

[i] For comparison, air-saturated water (ASW) at 1 atm pressure and a temperature of 18°C (after *Weiss* [1971] and *Benson and Krause* [1980]).

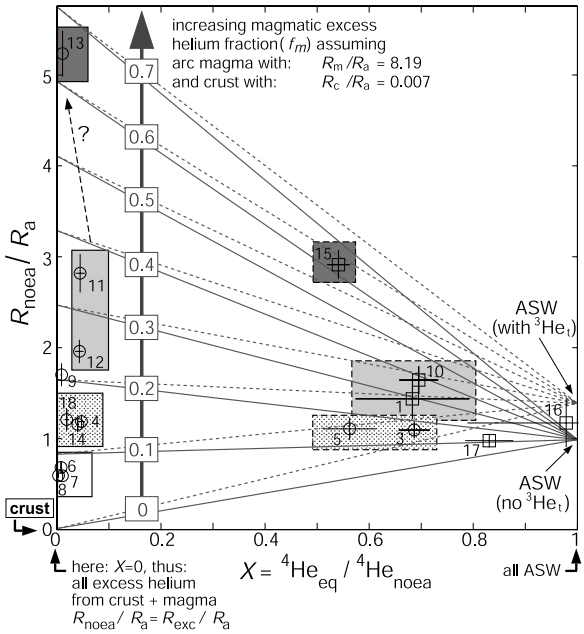

Figure 3. Mixing lines (ML) between air-saturated water (ASW) and water containing He_{exc} from the crust and/or magma. Cold and hot springs are indicated by squares and circles, respectively. Dashed mixing lines indicate ^3He_t contributions from the complete decay of 10 TU (section 6.1). In Figures 3, 5, and 6, solid- and dashed-lined boxes comprise springs that suggest no mixing and mixing with ASW, respectively, and gray-shaded/dotted boxes indicate similar R_{exc}/R_a ratios (as provided in Figures 5 and 6 and as indicated by similar mixing lines). The fraction of ASW contribution is given by X (see also equation (9)), while excess (magmatic and crustal) He fractions are provided by $1 - X$. Magma fractions (f_m), labeled by the vertical arrow for both with (dashed ML) and without (solid ML) ^3He_t, are estimated with respect to total excess helium ($1 - X$). In contrast to purely sedimentary systems with comparably little magmatic and/or mantle helium, here in magmatic systems, slopes of mixing lines can be strongly negative and divergence of mixing lines for $X \rightarrow 0$ can be significant. As a result, large slopes and divergences of mixing lines can cause significant He_{eq} corrections and increases in error bars, respectively, when projecting R_{noea}/R_a to $R_{noea}/R_a = R_{exc}/R_a$ (for $X = 0$) along mixing lines.

significantly different from R_{noae}/R_a and R_{meas}/R_a (Figure 3 and last two columns in Table 3). Thus discussion of the effects of our correction method is critical only for these three cold springs (1, 10, 15), all located on the eastern flanks of the Oregon Cascades (Figures 1 and 2). As shown in section 7.2, applying this approach to springs 1, 10, and 15 allows for an improved understanding of magmatic and hydrologic processes in the Cascades system. However, our combined method also yields estimates for magmatic excess helium fractions (f_m), thus providing useful volcanological insight for all samples even if atmospheric He contributions are low so that He/Ne corrections could be employed to remove atmospheric He components.

[19] To a first order, the fraction of magmatic (f_m) versus crustal ($1 - f_m$) contributions to He_{exc} is indicated by the slope of the mixing lines. We note that in active volcanic systems with significant magmatic excess helium fractions (f_m), slopes of mixing lines in Figure 3 are negative, a characteristic not observed in sedimentary basins [e.g., *Castro et al.*, 2000; *Kulongoski et al.*, 2003; *Castro*, 2004], where this type of analysis is commonly applied. Equation (9) requires estimation of representative crustal (R_c) and magmatic (R_m) end-member ratios, as well as ^3He_t production for the area of interest.

[20] Crustal R_c ratios vary over one order of magnitude. Characteristic crustal He production (e.g., for silicic rocks) results in $0.02 \leq R_c/R_a \leq 0.05$, while typical in situ production in sedimentary aquifers yields $0.001 \leq R_c/R_a \leq 0.005$ [e.g., *Castro*, 2004]. The Cascades are expected to yield a crustal end-member ratio of $R_c/R_a \approx 0.007$ based on mineral abundances in andesitic rocks [*Parker*, 1967], although dispersed dacitic domes and lava flows [e.g., *Ingebritsen et al.*, 1994] could increase this ratio slightly. In contrast, mid-ocean ridge basalts (MORBs) display $R_m/R_a = 8 \pm 1$ [*Farley and Neroda*, 1998]. Helium isotopic ratios integrated over total volcanic arc widths result in $R_m/R_a = 5.37 \pm 1.87$ [*Hilton et al.*, 2002]. The latter ratio is somewhat lower than typical MORB values and depends strongly on the distance to volcanic summits with maxima occurring at volcanic centers [e.g., *Marty et al.*, 1989; *van Soest et al.*, 1998; *Hilton et al.*, 2002; *Mariner et al.*, 2003]. The Cascades volcanic arc averages $R_m/R_a = 6.07 \pm 1.93$ [*Hilton et al.*, 2002]. We consider the maximum reported Cascades value of $R_m/R_a \approx 8.19$ [*Dodson and Brandon*, 1999] as our magmatic end member. Furthermore, we assume $^3He_t = 2.5 \times 10^{-14}$ cm^3 STP/g from the complete decay of 10 TU based on measurements by *James et al.* [2000] (Figure 3).

6.2. Comparison of Our Combined Analysis With Standard He/Ne Corrections

[21] Total atmosphere-normalized He/Ne ratios (equation (7)), without additional consideration of N_2/Ar ratios, are commonly used to correct

R_{meas}/R_a ratios for dissolved atmospheric He contributions [e.g., *Hilton*, 1996] by employing

$$\frac{R_{cor}}{R_a} = \frac{(\beta\Lambda R_{meas}/R_a) - 1}{\beta\Lambda - 1}, \qquad (13)$$

where $\beta = 1$ and $\beta = \beta_{Ne}/\beta_{He}$ for $R_{cor} = R_{cea}$ and $R_{cor} = R_{ceq}$, respectively. Here, β_{Ne} and β_{He} are the temperature-dependent Bunsen coefficients for the solubilities of Ne and He in water, respectively, assuming 0% salinity. $R_{cor} = R_{cea}$ denotes corrections where complete dissolution of air bubbles (i.e., excess air) are considered only (i.e., $\beta = 1$). In contrast, $R_{cor} = R_{ceq}$ assumes only ASW equilibration where the solubilities of atmospheric He and Ne into water depend on β_{He} and β_{Ne}, respectively.

[22] As stated in the previous section and illustrated by Figure 3 and Table 3, only samples 1, 10, and 15 have R_{exc}/R_a ratios distinct from R_{noea}/R_a (as illustrated by projections along mixing lines). Consequently, for these three samples the ability to deconvolve atmospheric helium concentrations (He_{da}) into their He_{eq} and He_{ea} components (equation (1)) is critical in order to remove the correct He_{eq} concentrations when determining He_{exc} and R_{exc}/R_a (section 6.1). The use of Ne, Ar, Kr, and Xe [*Ballentine and Hall*, 1999] provides best estimates (in a least-squares sense) for He_{ea} and He_{eq}. In contrast standard He/Ne corrections, without additional consideration of nitrogen for determination of N_2/Ar ratios do not allow distinction between He_{eq} and He_{ea}. *Hilton* [1996] shows that He/Ne ratios above approximately four times those present in the atmosphere ($\Lambda > 4$) do not require distinction between atmospheric He from A_{ea} and ASW and suggests assuming that all atmospheric helium (He_{da}) in fluid samples is a result of He_{eq}. In this case, $R_{cor} \approx R_{ceq}$ can be employed in equation (13) if recharge temperatures can be estimated independently. Indeed, Figure 4a shows that for samples with $X \approx 0$ (i.e., $\Lambda \gg 4$) R_{ceq}/R_a and R_{cea}/R_a are virtually identical to R_{noea}/R_a, which in turn is similar to R_{exc}/R_a where $X \approx 0$ because projections ($X \rightarrow 0$) can be neglected (section 6.1). For calculation of R_{ceq}/R_a we used best estimates (in a least-squares sense) of recharge temperatures as determined from Ne, Ar, Kr, and Xe measurements [*Ballentine and Hall*, 1999].

[23] As expected, He/Ne corrections that assume $He_{da} = He_{eq}$ only in equation (1) constitute lower bounds for R_{cor}/R_a (i.e., R_{ceq}/R_a, ∇ in Figure 4a)

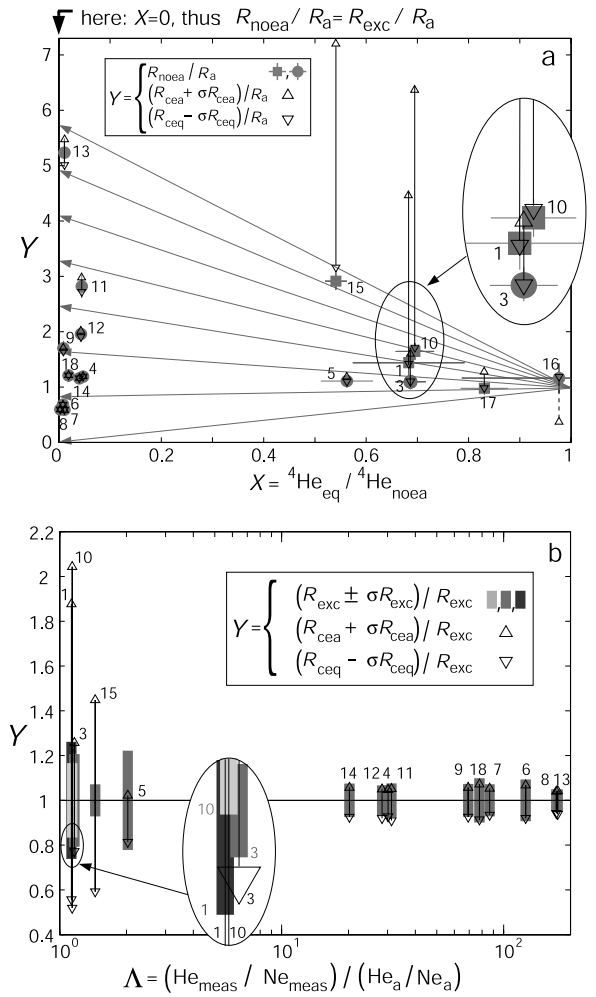

Figure 4. Comparison of results obtained from the He/Ne corrections with the combined approach that uses Ne, Ar, Kr, and Xe together with a He component mixing analysis (sections 6.1 and 6.2). (a) The x-axis as well as gray-shaded squares (cold springs) and circles (hot springs) are identical to R_{noea}/R_a values in Figure 3. Here Δ and ∇ represent upper $(R_{cea} + \sigma R_{cea})/R_a$ and lower $(R_{ceq} - \sigma R_{ceq})/R_a$ bounds of He/Ne-corrected samples, respectively, where the 1σ errors for each bound have been accounted for. X values for R_{ceq}/R_a and R_{cea}/R_a are not provided by the He/Ne correction so that X values from the combined method (equation (11), yielding X for R_{noea}/R_a ratios) are used for plotting purposes. Vertical error bars of R_{noea}/R_a are mostly covered by the ones for R_{cea}/R_a and R_{ceq}/R_a and their connecting lines but can be observed in Figure 3 and are represented here as gray-shaded bars. (b) R_{exc}, R_{cea}, and R_{ceq} ratios and their respective 1σ errors σR_{exc}, σR_{cea}, and σR_{ceq} normalized by R_{exc} where the latter is determined by the combined approach. Different shades of gray for $(R_{exc} \pm \sigma R_{exc})/R_{exc}$ are used for illustration purposes only so that bars with similar Λ values can be distinguished. Samples 16 and 17 have $\Lambda < 1$ and are thus not shown. A discussion of this figure is provided in section 6.2.

and thus agree with R_{noea}/R_a ratios as estimated using Ne, Ar, Kr, and Xe (gray squares and circles in Figure 4a). In contrast, assuming $He_{da} = He_{ea}$ only in equation (1) represents an upper bound for R_{cor}/R_a (i.e., R_{cea}/R_a, Δ in Figure 4a) as noted by *Hilton* [1996]. The actual fraction of He_{eq} versus He_{ea} also affects $X = {}^4He_{eq}/{}^4He_{noea}$ and thus determines our correction (i.e., the applicable mixing/projection line in Figure 4a) from R_{noea}/R_a to R_{exc}/R_a for $X \rightarrow 0$ when He_{eq} is removed. However, the value of X in Figure 4a is unknown for He/Ne-corrected samples and thus further corrections, such as projections along mixing lines, cannot be performed on R_{ceq}/R_a and R_{cea}/R_a (for illustrative purposes only, we plot R_{cor}/R_a values in Figure 4a at positions X determined by our combined method). As a result, the spread between upper (R_{cea}/R_a) and lower (R_{ceq}/R_a) bounds (Figure 4) represents the uncertainty for $R_{ceq}/R_a - \sigma R_{ceq}/R_a \leq R_{cor}/R_a \leq R_{cea}/R_a + \sigma R_{cea}/R_a$, where σ denotes the 1σ standard error of the parameter that follows. In contrast, removal of He_{eq} in addition to He_{ea}, using measurements of Ne, Ar, Kr, and Xe to constrain He_{eq} and He_{ea} [*Ballentine and Hall*, 1999], is illustrated by projections of mean R_{noea}/R_a values and their respective errors along mixing lines onto the left y-axis of Figures 3 and 4a, as discussed in section 6.1. Thus in our (latter) method the increase in error bars is illustrated by the divergence of mixing lines in Figures 3 and 4a (section 6.1).

[24] To illustrate the difference in uncertainties for R_{exc}/R_a (our method) and for R_{cor}/R_a (He/Ne method) for samples that show significant magmatic and atmospheric He contributions, we plot in Figure 4b Λ (equation (7)) versus $(R_{exc} \pm \sigma R_{exc})/R_{exc}$ (gray shaded bars) as well as $(R_{cea} + \sigma R_{cea})/R_{exc}$ (Δ) and $(R_{ceq} - \sigma R_{ceq})/R_{exc}$ (∇). Here, σR_{exc}, σR_{cea}, and σR_{ceq} are the 1σ standard errors of their mean values R_{exc}, R_{cea}, and R_{ceq}, respectively. As expected from Figure 4a, samples 1, 3, 5, 10, and 15–17 show a significant atmospheric He component ($X > 0.5$) resulting in $\Lambda < 4$ (section 5). Here, typically (except for sample 5) our method yields significantly smaller error bars than the standard He/Ne corrections (Figure 4b). Samples 16 and 17 yield $\Lambda < 1$ and are thus not shown in Figure 4b.

[25] Besides reducing uncertainties for R_{exc} (compared with R_{cor}), our combined approach (Figure 3) allows for estimation of magmatic versus crustal excess He fractions by providing estimates of f_m (equation (12)). Importantly, using our combined approach, it is possible to evaluate f_m for all samples, justifying the use of this method even in cases where $X \approx 0$ and thus $\Lambda \gg 4$ suggest that standard He/Ne corrections can sufficiently account for atmospheric He contributions.

7. Discussion of an Example Application Using the Combined Approach

[26] Here, we illustrate the practical gains achieved through the application of our combined approach (measuring Ne, Ar, Kr, and Xe and conducting He component mixing analyses) to the Oregon Cascades and the northwestern extents of the Basin and Range tectonic province (Figure 1). Section 7.1 discusses some general observations concerning the investigated springs. Sections 7.2 through 7.5 present specific findings regarding groundwater flow paths and/or magmatic He signals.

7.1. General Data Overview and Interpretation

[27] All springs except 17 and possibly 3 (Figure 5a) show $^3He_{exc}$ concentrations above values that could solely be obtained from the decay of 10 TU, the maximum value expected in the study region [*James et al.*, 2000]. $^3He_{exc}$ and $^4He_{exc}$ concentrations vary over more than two orders of magnitude (Figure 5, Table 3). In addition, results yield $0.5 \leq R_{exc}/R_a \leq 5.6$, well above all crustally produced ratios (Figures 5 and 6), suggesting that high excess helium concentrations are predominantly caused by magmatic helium contributions. Furthermore, our results show that (1) a number of samples yielding some of the lowest R_{exc}/R_a ratios (e.g., 6–9) present some of the highest excess He concentrations and are located at greater distances from the Cascades range (Figures 1 and 6), which could result from generally lower spring discharge rates in eastern Oregon (section 2); (2) samples suggesting negligible mixing with ASW (4, 6–9, 11–14, 18) (solid-lined boxes, Figure 3) present a wide range of $0.5 \leq R_{exc}/R_a \leq 5.6$, showing a dependence on distance to the volcanic arc (Figure 6) as reported previously for the Japanese volcanic arc [*Marty et al.*, 1989] and elsewhere [e.g., *van Soest et al.*, 1998; *Hilton et al.*, 2002].

[28] Generally [e.g., *James et al.*, 2000], excess He ratios in groundwaters with $R_{exc}/R_a > 1$ are interpreted as indicators of a significant magmatic He component. $R_{exc}/R_a \ll 1$ is typically interpreted as indicative of a dominant crustal component with

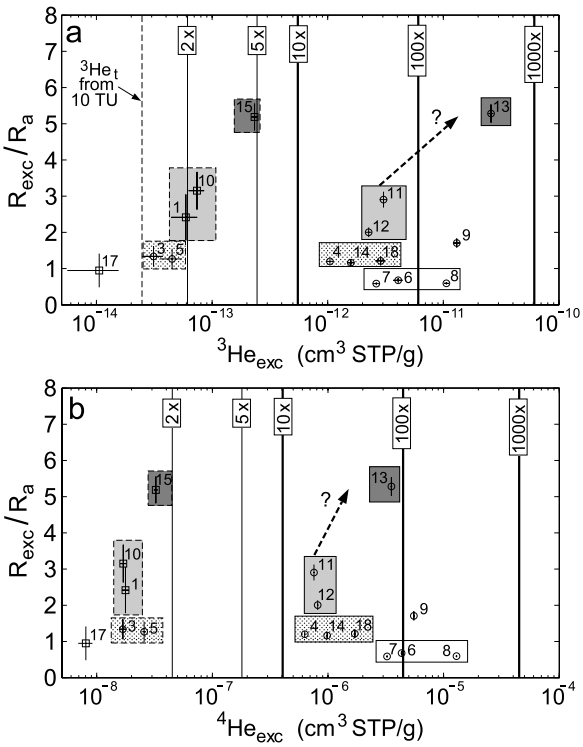

Figure 5. Excess He concentrations versus R_{exc}/R_a as obtained from the projection along mixing lines onto the left y-axis in Figures 3 and 4a, where $X = 0$ and thus $R_{noea}/R_a = R_{exc}/R_a$. Cold and hot springs are indicated by squares and circles, respectively. Vertical solid lines indicate 2×, 5×, 10×, 100×, and 1000× the ASW value at 1 atm pressure and 18°C [*Weiss*, 1971].

negligible mantle or magmatic contributions [e.g., *Castro et al.*, 1998a]. However, *Castro* [2004] shows that R_{exc}/R_a in groundwater samples are minimum bounds for the fraction of magmatic or mantle-derived He due to a generally strong dilution of the original signal by crustally produced He with significantly lower He isotopic ratios of $R_c/R_a \ll 1$ (section 4). Thus while in the absence of ^{3}He$_t$ production, $R_{exc}/R_a > 1$ can safely be interpreted as having a significant mantle or magma component, $R_{exc}/R_a \ll 1$ does not necessarily imply a lack thereof. Conversely, while $R_{exc}/R_a \approx 1$ can represent a mixture of magmatic and crustal He, it is also possible that $R_{exc}/R_a \approx 1$ in shallow groundwater with short residence times (so that $He_{cin} \rightarrow 0$) represents simply a pure ASW helium component. The latter is possible if shallow/local water is shielded by deeper/regional groundwater (Figure 2) from influx of external crustal (He_{cext}) and magmatic (He_m) helium. He shielding is most effective when deep groundwater fluxes are large, as demonstrated for some multilayered aquifer systems [*Castro et al.*, 1998b]. Thus to distinguish between shallow/local and deep/regional groundwater flow, which can potentially both yield similar R_{exc}/R_a values, it is critical to also consider He_{exc} concentrations and to employ a component mixing analysis (section 6.1), as discussed next.

7.2. Shallow Versus Deep Groundwater Flow and Magmatic He Contributions to the Eastern Cascades

[29] While spring 16 is clearly representative of ASW, spring 17 contains some excess helium, of which ^{3}He$_{exc}$ can potentially result from tritium decay alone (Figures 3 and 5a) and ^{4}He$_{exc}$ (∼18% as indicated by $1 - X$ in Figure 3) appears to be of crustal origin. Thus springs 16 and 17 likely represent shallow groundwater flow that is at least partially shielded from external crustal and/or magmatic excess He by deep groundwater flow (Figure 2). Indeed, springs 1, 10, and 15 (Figures 1 and 2) may represent such deep groundwater flow advecting most (or all) available magmatic (and external crustal) He_{exc} and being subsequently mixed with shallow ASW (Figure 3). To obtain the original "unmixed" source R_{exc}/R_a ratios for springs 1, 10, and 15 (Figures 5 and 6), we remove

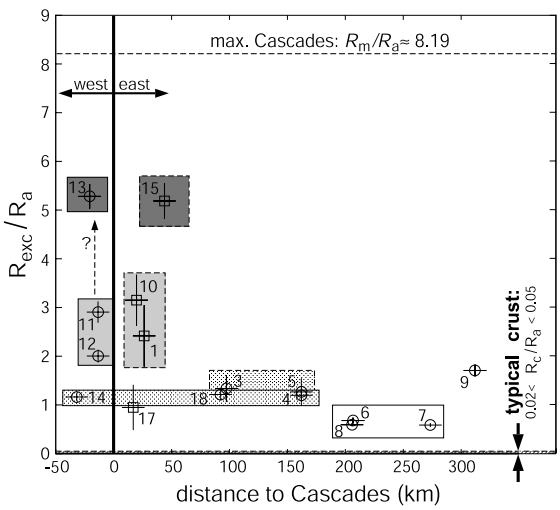

Figure 6. R_{exc}/R_a versus distance to the Cascades. Cold and hot springs are indicated by squares and circles, respectively. Discussion of mid-ocean ridge basalt, volcanic arc, and crustal R_{exc}/R_a ratios are provided for comparison in the main text. A maximum ratio of $R_m/R_a = 8.19$ (from samples of xenolith cores at Simcoe volcano, Washington) has been reported [*Dodson and Brandon*, 1999] for the Cascades (upper dashed horizontal line). Typical $0.02 < R_c/R_a < 0.05$ ratios for the crust are discussed in section 6.1.

the ASW helium component (He_{eq}) from He_{noea}, as described in section 6.1 and illustrated in Figure 3.

[30] Spring River (15) shows the largest difference between R_{noea} and R_{exc} (Figures 3 and 5), demonstrating the importance of accounting for ASW helium components (He_{eq}). In fact, once the He_{eq} component is removed, sample 15 shows $R_{exc}/R_a \approx 5.2$, comparable to Austin Hot Springs (13) on the western side of the Cascades (Figure 6), where the largest off-summit (away from volcanic centers) magmatic He and heat signals are typically observed [e.g., *Ingebritsen et al.*, 1994; *Evans et al.*, 2004]. On the eastern side of the Cascades, off-summit magmatic He signals reach values of up to $\sim$4.6 R_a [e.g., *Evans et al.*, 2004]. Otherwise, high He isotopic ratios of >6 R_a are commonly restricted to volcanic centers on (e.g., Mt. Baker, Mt. Hood, Mt. Shasta, and Lassen Peak [*Mariner et al.*, 2003]) or close to (e.g., Newberry volcano [*Mariner et al.*, 2003] and Simcoe volcano [*Dodson and Brandon*, 1999]) the volcanic arc, as noted in section 6.1. Both springs (13, 15) suggest a very high magmatic excess helium fraction of $0.6 \leq f_m \leq 0.7$, as defined in equation (12). Springs feeding Wood (1) and Metolius (10) rivers (Figures 1 and 2) also show $R_{noea} \not\approx R_{exc}$ with $1.8 \leq R_{exc}/R_a \leq 3.6$ (Figures 5 and 6) and a lower-bound $0.20 \leq f_m \leq 0.45$ (Figures 3), similar to Breitenbush Hot Springs (11, 12) west of the Cascades (Figures 1 and 2).

[31] Assuming short residence times so that in situ production of He_{cin} is negligible, the previous observations suggest that magmatic He contributions to groundwater beneath the eastern flanks of the Cascades are comparable to the ones under the western flanks but that mixing with ASW masks such high magmatic He contributions on the eastern side. This result is similar in nature to *Manga* [1998], who finds significant, but also largely diluted, magmatic heat signals in some cold springs east of the Cascades crest, including Metolius (10) and Spring (15) rivers (Figures 1 and 2). These inferences for groundwater flow patterns are also in accordance with *James et al.* [2000], suggesting deep flow to springs feeding Metolius (10) and Spring (15) rivers and shallow flow to springs discharging into Fall (16) and Quinn (17) rivers (Figures 1 and 2).

7.3. Springs >70 km East of the Cascades

[32] When mixing lines (Figure 3) are approximately horizontal, as for springs 3 and 5, $R_{noea}/R_a \approx R_{exc}/R_a \approx 1$ so that removing the significant ASW helium component has a negligible impact on R_{exc}/R_a. However, Figures 3 and 5 suggest that at least some magmatic He_{exc} contributes to the roughly 30% and 45% excess (both magmatic and crustal) helium ($1 - X$ in Figure 3) in springs 3 and 5, respectively. Spring 3 shows $^3He_{exc}$ concentrations only slightly above those that could be expected from maximum tritium decay in the region (dashed lines in Figures 3 and 5a). Therefore depending on the tritium contribution to ^{3}He, a magmatic excess helium fraction of $0.03 \leq f_m \leq 0.20$ (equation (12)) to spring 3 may be expected (Figure 3). Similarly, spring 5 may exhibit $0.08 \leq f_m \leq 0.20$ (Figure 3). Therefore spring 5 (and possibly spring 3) have a similar original magmatic He signal as nearby springs 4 and 18 (Figure 1) which show $1 \leq R_{exc}/R_a \leq 1.6$ (Figures 5 and 6) and $0.13 \leq f_m \leq 0.17$ (Figure 3). In general, springs at distances >70 km east of the Cascades (3–9, 18) show significant He_{exc} (Figure 5), lower bound $0.05 \leq f_m \leq 0.22$ (Figure 3), and $0.5 \leq R_{exc}/R_a \leq 1.8$ (Figures 3 and 6).

[33] Such high magma signals may be expected in eastern Oregon, considering the proximity of relatively recent magmatic and ongoing tectonic activity in the Basin and Range and the Snake River Plain (Figure 1). However, it is unclear how long magmatic helium signals can prevail in groundwater systems [*Clauser et al.*, 2002]. An alternative hypothesis for elevated He isotopic ratios in the Basin and Range might be related to the presence of active normal faults [e.g., *Hammond and Thatcher*, 2004]. These faults could provide "pathways" that promote rapid He transfer from the, here very shallow, mantle minimizing mixing with crustally produced radiogenic ^{4}He.

[34] Independent of the cause, by employing a He component mixing analysis providing magmatic excess He fractions of up to $f_m \approx 0.22$ (Figure 3), we show that magmatic and/or mantle contributions are larger than might be inferred from $0.5 \leq R_{exc}/R_a \leq 1.8$ ratios alone (Figures 5 and 6 and Table 3). Indeed, R_{exc}/R_a ratios alone do not discern between magmatic and crustal excess He contributions.

7.4. Springs West of the Cascades

[35] Hot springs (11–14) west of the Cascades crest typically discharge along faults near the boundary between the Western and the High Cascades (Figure 2, section 2). Figures 3 and 5 indicate negligible mixing with ASW, high He_{exc}, and a wide range of $1 \leq R_{exc}/R_a \leq 5.6$. Higher

ratios (dashed arrows in Figures 3, 5, and 6) of $5 \leq R_{exc}/R_a \leq 7$ may be expected for Breitenbush Hot Springs (11, 12) based on previous publications [e.g., *Ingebritsen et al.*, 1994]. Causes for this discrepancy are not clear. Reduced R_{exc}/R_a ratios in the collected pure water phase could be due to the observed presence of a gas phase in these springs into which He could partition preferentially [e.g., *Shaw et al.*, 2003]. Another reason for lower R_{exc}/R_a ratios may be a temporal decrease in magmatic and/or increase in crustal He flux, although the Cascades hydrothermal system appears to be close to steady state [*Ingebritsen et al.*, 2001].

[36] In contrast, low $R_{exc}/R_a \approx 1.2$ for Bagby Hot Springs (14) are also documented by *Ingebritsen et al.* [1994] and are attributed to their (partial) isolation from the Quaternary arc by a drainage divide and deep local circulation (Figures 1 and 2) through older and lower permeability strata of the Western Cascades (section 2). Here, reduction in R_{exc}/R_a ratios could be a result of longer residence times in the older, less permeable, and more radiogenic helium-rich sediments, diluting (possibly by the drainage divide already reduced) magmatic He signals. We exclude significant dilution of Bagby Hot Springs (14) by dissolved atmospheric He components because $He_{da}/He_{meas} = 0.039 < 0.5$ is low, $\Lambda = 20.2 > 4$ is high (Table 3), and excess He concentrations are significant (Figure 5).

[37] Our result of $R_{exc}/R_a = 5.3 \pm 0.3$ for Austin Hot Springs (13) agrees with 5.7 reported by *Ingebritsen et al.* [1994]. Most importantly, magmatic He_{exc} fractions for hot springs 11–14 are significant and show a lower bound range of $0.15 \leq f_m \leq 0.70$ (Figure 3), similar to f_m values now determined (section 7.2, Figure 3) for cold springs (1, 10, 15) east of the Cascades crest (Figure 1). Figure 2 summarizes our conceptual model of the groundwater flow paths in the Oregon Cascades inferred from the helium analysis discussed in this section.

7.5. Faults, Hot Springs, and Reduced ASW Mixing

[38] Hot springs (4, 6, 11–14, 18) with significant magmatic He and negligible mixing with ASW (Figures 3 and 5) may be the result of deep, heated groundwater that ascends quickly to the surface along faults (Figure 2) that remain permeable by hydroseismicity [*Saar and Manga*, 2003]. Discharge of hot water at springs requires a permeability range of $10^{-17} \leq k \leq 10^{-15}$ m^2 [*Forster and Smith*, 1989]. Lower k allows for temperature equilibration with the surrounding rock during slow water ascent and larger k tends to dilute both heat and excess He signals. Hot spring discharge along (active) normal faults, often forming topographic lows promoting spring discharge [e.g., *Ingebritsen and Sanford*, 1998], occurs both in the Cascades [e.g., *Saar and Manga*, 2004] (Figure 2) and in the extensional tectonic setting [e.g., *Hammond and Thatcher*, 2004] of the Basin and Range [e.g., *McKenna and Blackwell*, 2004]. In contrast, near-surface mixing between deep and shallow water and resulting cold water discharge may occur preferentially at springs not associated with faults.

8. Concluding Remarks

[39] We show that it is critical to consider mixing of He components (Figure 3) as well as He isotopic concentrations (Figure 5) and ratios (Figure 6) when inferring magmatic or mantle He contributions to groundwater. Investigating He component mixing (sections 6.1 and 7.2 and Figure 3) is particularly important when strong dilution of potentially significant excess He components by atmospheric He is suspected for example from atmosphere-normalized He/Ne ratios < 4. This is crucial as magmatic and mantle He components in groundwaters are typically lower bounds reducing the apparent magma or mantle He signal. In addition, combining Ne, Ar, Kr, and Xe measurements with He component mixing analyses provides a means to estimate magmatic versus crustal excess He fractions (f_m) for all samples (sections 7.2, 7.3, and 7.4). Our examples from the magmatically active Oregon Cascades and from eastern Oregon demonstrate that such an analysis can provide additional insight into magmatism and groundwater flow patterns.

Appendix A: General Noble Gas Measurement and Signal Strength Characteristics

[40] Noble gas measurements were performed at the University of Michigan. The noble gas sample container is attached to a vacuum extraction system and noble gases are quantitatively extracted for inletting into a MAP215 mass spectrometer. Noble gases are transported using water vapor as a carrier gas through two constrictions in the vacuum system, purified, and sequentially allowed to enter a MAP215 mass spectrometer using a cryo-separator as described below.

[41] The mass spectrometer is equipped with both a Faraday detector and an electron multiplier. The Faraday detector has a preamplifier with a $10^{11}\Omega$ resistor and the electron multiplier operates in ion counting mode. An adjustable width collector slit has been installed in front of the electron multiplier so that ^{3}He can be resolved from the HD molecule. For the initial pipette analysis procedure outlined below, the typical signal sizes at masses 4, 20, 40, 84, and 132 are 0.04, 0.25, 2.4, 0.005, and 0.00035 V on the Faraday detector. Kr and Xe are measured on the electron multiplier and their signal sizes have been scaled to the equivalent Faraday detector values. The ion source is a Nier type source operated at 500 μA electron trap current. When the ^{3}He/^{4}He ratio is measured, there is a signal of ~2.4 V on the Faraday detector at mass 4 and a signal of ~120 ions/s on the electron multiplier.

Appendix B: Noble Gas Data Reduction and Interpretation

[42] Concentration estimates (in cm^3 STP/g) for He, Ne, Ar, Ke, and Xe have standard errors of 1.5, 1.3, 1.3, 1.5, and 2.2%, respectively. From concentrations of Ne, Ar, Kr, and Xe (and their error estimates) paleotemperatures for the water samples were estimated following *Ballentine and Hall* [1999]. Data was fitted using both the spring elevation and presumed recharge elevations derived from oxygen isotope data, where a relationship between δ^{18}O (measured separately at Lawrence Livermore National Laboratory) and elevation has been established for parts of the Cascades [*James et al.*, 2000]. In many cases, low measured Xe concentrations amply demonstrate that there has been significant reequilibration of the noble gases with air at elevated spring temperatures. From the fitted paleotemperature, we estimate both the trapped air He as well as the ASW he component. This estimate is in turn used to calculate the R/R_a value for the excess He component. However, due to the trade-off between elevation (i.e., air pressure) and fitted noble gas temperature values, the predicted He concentration from trapped air and ASW components for assumed recharge and discharge elevations are virtually identical and are thus averaged, resulting in 1σ standard deviations below 0.02 R_{exc}/R_a for each sample.

[43] Replicate water samples were analyzed for noble gas concentrations and isotopic ratios for all springs except 4, 5, 7, 11, and 12. Only maximum He_{exc} values are reported for replicates as lower bounds because any sampling artifacts or loss of noble gases either before or after sampling will tend to reduce the measured He_{exc} value.

Appendix C: Noble Gas Extraction Line and Measurement Procedures

[44] The noble gas extraction and purification system (Figure C1) at the University of Michigan uses similar principles as that at Lamont-Doherty Earth Observatory (LDEO) at Columbia University [e.g., *Stute et al.*, 1995]. The extraction and purification system at the University of Michigan consists of four zones: zone 1 consists of an attachment point for the Cu sample tube and a low-diffusion glass flask; zone 2 is connected to zone 1 via a 4 cm length of standard 1/16″ stainless steel tubing and the zone has a stainless steel liquid nitrogen cold trap; zone 3 contains a canister of 3 Å molecular sieve and is connected to zone 2 through a 1 mm orifice; zone 4 comprises the main clean-up part of the system and has connections to a Ti sponge getter and an Air Products model CS202W cryo-separator whose temperature is controlled by a Scientific Instruments model 9700 controller. Temperature regulation at any point is at least within 0.05 K and usually within 0.01 K of the set point. Zones 1 through 3 share a common turbo vacuum pump system and are connected to each other with manually actuated Nupro 4BG bellows valves. An air pipette system is connected to zone 3. The air pipette and all of the valves in zone 4 use pneumatically actuated Nupro 4BG valves under computer control.

[45] A single 14 g water sample is used to estimate the noble gas concentrations of He, Ne, Ar, Kr, and Xe, as well as the isotopic ratios of these elements, including the ^{3}He/^{4}He ratio. Noble gas concentrations are estimated by comparing the mass spectrometer signal strength for the sample with a standard air sample that can be introduced into zone 3. The air pipette reservoir was loaded with outdoor air into a known volume. The air was subsequently dried with 3 Å molecular sieve zeolite and its pressure was measured using a capacitive manometer. The depletion of the air reservoir is automatically monitored by the computer control software.

[46] The measurement sequence starts with a complete set of isotope measurements of an air pipette aliquot that is introduced directly into zone 3. Approximately 2% of the 0.1882 ml air sample is

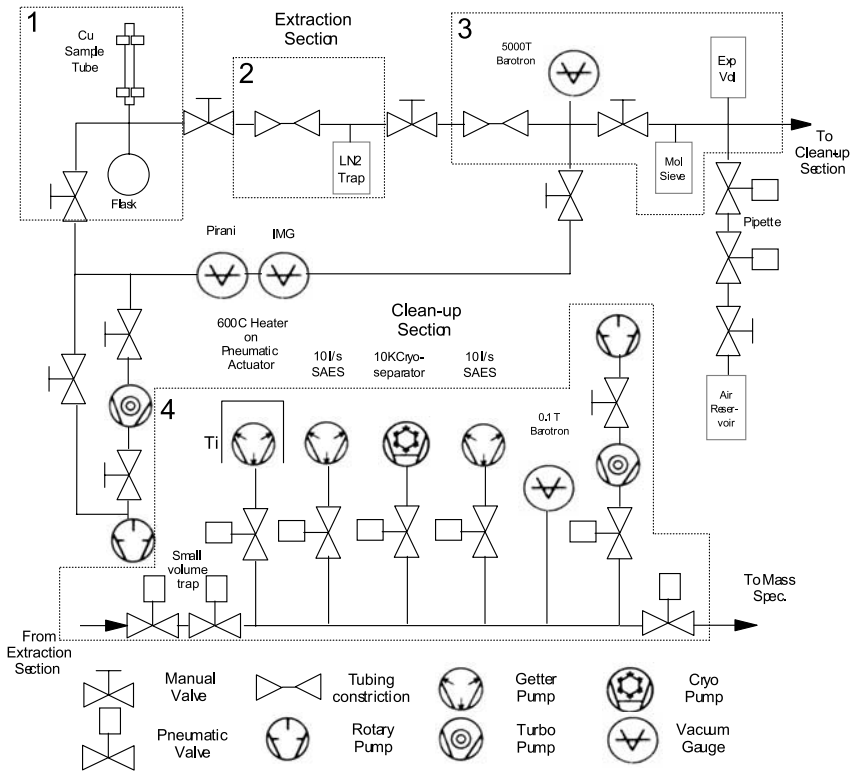

Figure C1. Schematic of the noble gas extraction and purification line. A description is provided in Appendix C.

trapped in a small volume between 2 valves connecting zones 3 and 4. This volume is introduced into zone 4 and the remainder of the gas in zone 3 is pumped out. The air sample is gettered using a Ti sponge at 600°C and a small portion of the cleaned noble gas is retained in the small volume between zones 3 and 4 for later measurement of the Ar isotopes. The majority of the sample is then pumped into the cryo-separator, which has been precooled to an indicated T of 35 K. At this indicated T, He is released, while all other noble gases are trapped. The He is then introduced into the mass spectrometer and its signal strength at mass 4 is determined. This He measurement is used strictly for the He concentration estimate, as there is insufficient He at this stage for measurement of ^{3}He.

[47] The cryo-separator is then warmed to an indicated T of 65 K and Ne is released into the mass spectrometer. Interference from doubly charged ^{40}Ar and CO_2 is monitored by measurements at masses 40 and 44 as well as the Ne isotopes at 20, 21, and 22. During Ne measurements, the cryo-separator is warmed further to 180 K. The Ar measurement is made on the small amount of gas that is trapped between zones 3 and 4. This gas is expanded into the zone 4 manifold, and only about 4% of this gas is inlet into the mass spectrometer. During the Ar measurements, the bulk of the original sample's Ar is pumped out of the cryo-separator at 180 K. After the Ar is purged from the system, zone 4 is again isolated from its turbo pump and allowed to warm to 215 K, releasing the pipette sample's Kr. Xe is released in the T range of 215 to 270 K, and the whole system is pumped out for 10 minutes with the cryo-separator held at 280 K. Once cleaned out, the system is cooled again to 35 K in preparation for analyzing the water sample. He, Ne, and Ar isotopes are measured using a Faraday detector, and Kr and Xe are measured using an electron multiplier in ion counting mode.

[48] While the air pipette sample is being analyzed for He, Ne, Ar, Kr, and Xe, the water sample is prepared in zones 1 through 3. Once the Cu tube is attached to zone 1, that region is pumped down to at least 2×10^{-3} Torr. Once this pressure is achieved, the system is isolated from the pump, the lower clamp is released, and the water sample is allowed to flow into the glass flask. The Cu tube is heated to make sure that all of the water is released from the tube. The water is stirred for

30 min and then the valve between zones 1 and 2 is opened, with liquid N_2 on the cold trap in zone 2. Noble gases and water vapor are pumped into the cold trap for 30 min. The capillary tube is equipped with a heater to avoid the possibility of gas transfer being blocked due to condensation of water in the capillary. After this transfer, the valve is closed and the cold trap is warmed to room temperature. Transfer of the noble gases to zone 3 is achieved by opening the valve between zone 2 and zone 3 for 5 s. This transfer procedure is repeated four additional times to ensure that all noble gases are pumped by water vapor into zone 3 through the 1 mm orifice. At this point, the water sample's noble gases are in the same volume and at the same T as the original air pipette sample. Once the air sample's mass spectrometer analyses are finished, and the cryo-separator has cooled back to 35 K, the same procedure is repeated for 2% of the water sample's noble gases.

[49] Before the mass spectrometer runs can be started, the noble gas pressure in zone 4 is kept to within about 60% of that produced by the air pipette sample (about 4×10^{-3} Torr). This pressure is monitored using a 0.1T full-scale capacitive manometer, and if necessary, about 46% of the gas is trapped in part of the system and the remainder pumped out. This is repeated as many times as necessary to reduce the pressure enough so that the sample's pressure is similar to that of the air pipette run. The He, Ne, Ar, Kr, and Xe concentrations are estimated using the ratio of sample to pipette at masses 4, 20, 36, 84, and 132, modified by the pressure reduction factor needed to get the sample near the same total pressure as the air pipette run.

[50] The above procedure was tested and calibrated with synthetic laboratory samples produced at a known temperature. Initially, we consistently had a low measured concentration for the heavy noble gases (Kr and especially Xe). We have corrected our first set of analyses based on the measured recovery efficiency. Low measured Xe concentrations were likely due to the presence of a small quantity of sintered steel in the mass spectrometer inlet which had been introduced for the measurement of small quantities of Ne in the presence of Ar. We speculate that the presence of higher H_2 and H_2O partial pressures may have caused enhanced adsorption of heavy noble gases. Once the sintered steel was isolated from the system, this behavior disappeared and the correction for incomplete Kr and Xe recovery is no longer needed.

[51] Only about 2% of the noble gas sample is introduced for the gas concentration measurement. The remaining 98% is retained in zone 3 for measurement of the $^3He/^4He$ ratio. The cryo-separator is cooled once again, this time to minimum T (below about 10 K) at which point He is pumped. From the He concentration information in the first He measurement, an inlet strategy is determined to allow for a ^4He signal between about 1 and 3V on the Faraday detector. After gettering with the Ti sponge at 600°C, the Ti sponge furnace is automatically lowered to cool the Ti and reduce the amount of hydrogen that is inlet into the mass spectrometer. The ^3He and HD peaks are measured using the electron multiplier and the ^4He peak is measured using the Faraday detector. After the sample is inlet, zones 3 and 4 are pumped out and readied for an air $^3He/^4He$ measurement on an air pipette sample. The R/R_a value is determined by the ratio of the apparent $^3He/^4He$ values for the sample and the air run.

[52] During the sample mass spectrometer runs, the liquid water in zone 2 is returned to zone 1 by freezing the water back through the capillary into the glass flask. Once the flask is back at room temperature, the flask is removed from the system and the water is weighed. This mass value is used to estimate the noble gas concentrations.

Acknowledgment

[53] Support by the University of Michigan and a Turner Postdoctoral Fellowship as well as a University Collaborative Research Program (UCRP) award through the Center for Accelerator Mass Spectrometry (CAMS) at Lawrence Livermore National Laboratory (LLNL) is greatly appreciated. We would like to extend special thanks to M. van Soest and an anonymous reviewer, as well as to associate editor D. Hilton whose insightful and detailed comments and suggestions greatly benefited the final version of this manuscript. We also thank M. Wenzel for his contributions in the field. The shaded relief map was made using the Generic Mapping Tools (GMT) and digital elevation models (DEMs) from the USGS.

References

Ballentine, C. J., and C. M. Hall (1999), Determining paleotemperature and other variables by using an error-weighted, nonlinear inversion of noble gas concentrations in water, *Geochim. Cosmochim. Acta*, *63*(16), 2315–2336.

Benson, B. B., and D. Krause (1980), Isotopic fractionation of helium during solution: A probe for the liquid-state, *J. Solution Chem.*, *9*(12), 895–909.

Castro, M. C. (2004), Helium sources in passive margin aquifers: New evidence for a significant mantle ^3He source in aquifers with unexpectedly low in situ $^3He/^4He$ production, *Earth Planet. Sci. Lett.*, *222*(3–4), 897–913.

Castro, M. C., A. Jambon, G. de Marsily, and P. Schlosser (1998a), Noble gases as natural tracers of water circulation in the Paris Basin: 1. Measurements and discussion of their origin and mechanisms of vertical transport in the basin, *Water Resour. Res.*, *34*(10), 2443–2466.

Castro, M. C., P. Goblet, E. Ledoux, S. Violette, and G. de Marsily (1998b), Noble gases as natural tracers of water circulation in the Paris Basin: 2. Calibration of a groundwater flow model using noble gas isotope data, *Water Resour. Res.*, *34*(10), 2467–2483.

Castro, M. C., M. Stute, and P. Schlosser (2000), Comparison of ^{4}He ages and ^{14}C ages in simple aquifer systems: Implications for groundwater flow and chronologies, *Appl. Geochem.*, *15*(8), 1137–1167.

Clarke, W. B., W. Jenkins, and Z. Top (1976), Determinations of tritium by mass-spectrometric measurement of ^{3}He, *Int. J. Appl. Radiat. Is.*, *27*(9), 515–522.

Clauser, C., E. Griesshaber, and H. Neugebauer (2002), Decoupled thermal and mantle helium anomalies: Implications for the transport regime in continental rift zones, *J. Geophys. Res.*, *107*(B11), 2269, doi:10.1029/2001JB000675.

Dodson, A., and A. Brandon (1999), Radiogenic helium in xenoliths from Simcoe, Washington, USA: Implications for metasomatic processes in the mantle wedge above subduction zones, *Chem. Geol.*, *160*(4), 371–385.

Evans, W. C., M. C. van Soest, R. H. Mariner, S. Hurwitz, S. E. Ingebritsen, C. W. Wicks Jr., and M. E. Schmidt (2004), Magmatic intrusion west of Three Sisters, central Oregon, USA: The perspective from spring geochemistry, *Geology*, *32*(1), 69–72.

Farley, K. A., and E. Neroda (1998), Noble gases in the Earth's mantle, *Annu. Rev. Earth Planet. Sci. Lett.*, *26*, 189–218.

Forster, C., and L. Smith (1989), The influence of groundwater flow on thermal regimes in mountainous terrain: A model study, *J. Geophys. Res.*, *94*, 9439–9451.

Graham, D. (2002), Noble gas isotope geochemistry of mid-ocean ridge and ocean island basalts: Characterization of mantle source reservoirs, in *Noble Gases in Cosmochemistry and Geochemistry*, vol. 47, edited by D. Porcelli, C. J. Ballentine, and R. Wieler, pp. 247–317, Mineral. Soc. of Am., Washington, D.C.

Hammond, W., and W. Thatcher (2004), Contemporary tectonic deformation of the Basin and Range province, western United States: 10 years of observation with the Global Positioning System, *J. Geophys. Res.*, *109*, B08403, doi:10.1029/2003JB002746.

Hilton, D. R. (1996), The helium and carbon isotope systematics of a continental geothermal system: Results from monitoring studies at Long Valley caldera (California, U.S.A.), *Chem. Geol.*, *127*(4), 269–295.

Hilton, D. R., T. Fischer, and B. Marty (2002), Noble gases and volatile recycling at subduction zones, in *Noble Gases in Cosmochemistry and Geochemistry*, vol. 47, edited by D. Porcelli, C. J. Ballentine, and R. Wieler, pp. 319–370, Mineral. Soc. of Am., Washington, D.C.

Ingebritsen, S. E., and W. E. Sanford (1998), *Groundwater in Geologic Processes*, 1st ed., 341 pp., Cambridge Univ. Press, New York.

Ingebritsen, S. E., R. H. Mariner, and D. R. Sherrod (1994), Hydrothermal systems of the Cascades range, north-central Oregon, *Prof. Pap. 1044-L*, U.S. Geol. Surv., Reston, Va.

Ingebritsen, S. E., D. L. Galloway, E. M. Colvard, M. L. Sorey, and R. H. Mariner (2001), Time-variation of hydrothermal discharge at selected sites in the western United States: Implications for monitoring, *J. Volcanol. Geotherm. Res.*, *111*(1–4), 1–23.

James, E., M. Manga, T. P. Rose, and G. Hudson (2000), The use of temperature and the isotopes of O, H, C, and noble gases to determine the pattern and spatial extent of groundwater flow, *J. Hydrol.*, *237*, 100–112.

Kulongoski, J., D. Hilton, and J. Izbicki (2003), Helium isotope studies in the Mojave Desert, California: Implications for groundwater chronology and regional seismicity, *Chem. Geol.*, *202*(1–2), 95–113.

Manga, M. (1998), Advective heat transport by low-temperature discharge in the Oregon Cascades, *Geology*, *26*(9), 799–802.

Mariner, R., W. Evans, T. Presser, and L. White (2003), Excess nitrogen in selected thermal and mineral springs of the Cascades Range in northern California, Oregon, and Washington: Sedimentary or volcanic in origin?, *J. Volcanol. Geotherm. Res.*, *121*(1–2), 99–114.

Marty, B., A. Jambon, and Y. Sano (1989), Helium isotopes and CO_2 in volcanic gases of Japan, *Chem. Geol.*, *76*(1–2), 25–40.

McKenna, J., and D. Blackwell (2004), Numerical modeling of transient basin and range extensional geothermal systems, *Geothermics*, *33*(4), 457–476.

Ozima, M., and F. A. Podosek (2002), *Noble Gas Geochemistry*, 2nd ed., 286 pp., Cambridge Univ. Press, New York.

Parker, R. L. (1967), Composition of the Earth's crust, in *Data of Geochemistry*, 6th ed., *Prof. Pap. 440-D*, pp. D1–D19, U.S. Geol. Surv., Reston, Va.

Rose, T. P., and M. L. Davisson (1996), Radiocarbon in hydrologic systems containing dissolved magmatic carbon dioxide, *Science*, *273*(5280), 1367–1370.

Saar, M. O., and M. Manga (2003), Seismicity induced by seasonal groundwater recharge at Mt. Hood, Oregon, *Earth Planet. Sci. Lett.*, *214*, 605–618.

Saar, M. O., and M. Manga (2004), Depth dependence of permeability in the Oregon Cascades inferred from hydrogeologic, thermal, seismic, and magmatic modeling constraints, *J. Geophys. Res.*, *109*, B04204, doi:10.1029/2003JB002855.

Shaw, A. M., D. R. Hilton, T. P. Fischer, J. A. Walker, and G. E. Alvarado (2003), Contrasting He-C relationships in Nicaragua and Costa Rica: Insights into C cycling through subduction zones, *Earth Planet. Sci. Lett.*, *214*, 499–513.

Stute, M., J. Clark, P. Schlosser, W. Broecker, and G. Bonani (1995), A 30,000 yr continental paleotemperature record derived from noble gases dissolved in groundwater from the San Juan basin, New Mexico, *Quatern. Res.*, *43*(2), 209–220.

van Soest, M. C., D. R. Hilton, and R. Kreulen (1998), Tracing crustal and slab contributions to arc magmatism in the Lesser Antilles island arc using helium and carbon relationships in geothermal fluids, *Geochim. Cosmochim Acta*, *62*(19–20), 3323–3335.

Weise, S. M., and H. Moser (1987), Groundwater dating with helium isotopes, in *Techniques in Water Resources Development*, pp. 105–126, Int. Atom. Energy Agency, Vienna.

Weiss, R. F. (1968), Piggyback sampler for dissolved gas studies on sealed water samples, *Deep Sea Res.*, *15*, 695–699.

Weiss, R. F. (1971), Solubility of helium and neon in water and sea water, *J. Chem. Eng. Data*, *16*, 235–241.